Jurnal Kejuruteraan 37(7) 2025: 3135-3149
https://doi.org/10.17576/jkukm-2025-37(7)-05

ABAQUS Scripting for Bone Microstructure Modeling and Cutting Analysis in Cortical Bones

Du Qianrui, Siti Sarah Kamaludin, Feizal Yusof, Inzarulfaisham Abd Rahim & Norwahida Yusoff*

School of Mechanical Engineering, Universiti Sains Malaysia, Malaysia

**Corresponding author: menorwahida@usm.my*

Received 15 November 2024, Received in revised form 22 June 2025
Accepted 22 July 2025, Available online 30 October 2025

ABSTRACT

Vibration-assisted cutting (VAC) has transitioned from industrial applications to orthopedic bone cutting. However, the anisotropic nature of bone complicates the process due to its intrinsic toughening mechanisms and susceptibility to surface damage. Finite element analysis (FEA) is widely used to evaluate cutting efficiency, but simulating tool-bone contact remains challenging due to large deformations causing convergence issues. To simplify modeling, this study develops a Python-based micro-modeling framework incorporating user-defined bone microstructure and porosity. Two models, representing young and aged bones, are validated by comparing stress intensity factors with analytical results for a single-edge notch bending (SENB) specimen, yielding a 4.5% deviation. Using the extended finite element method (XFEM), these models are used to examine the effects of amplitude and cutting depth on VAC performance. Results indicate that VAC reduces cutting force by up to 30.6% in aged bone compared to conventional cutting, with force reductions being more pronounced at higher amplitudes. Cutting stress is also reduced, particularly at 40 μm depth, where VAC decreases von Mises stress by 40.6% in aged bone and 9.63% in young bone. Crack propagation patterns show smoother and more controlled paths under VAC, particularly at shallow depths. Although VAC results in higher local cutting temperatures, the affected area is more confined, potentially leading to reduced chip sizes. These findings highlight VAC's potential to enhance orthopedic bone cutting by reducing force and stress while improving crack control and minimizing thermal damage.

Keywords: Vibration-assisted cutting; cortical bone; microstructure; crack propagation; extended finite element analysis

INTRODUCTION

Cortical bone, a dense and anisotropic composite material, plays a crucial role in structural support and load-bearing functions in the human body. However, its complex microstructure and mechanical behavior present significant challenges in orthopedic bone-cutting procedures. Improper cutting can lead to crack propagation, surface damage, and residual defects, which may compromise implant stability, delay healing, and cause long-term complications (Robles-Linares et al. 2021). Additionally, excessive thermomechanical loading during cutting can induce heat accumulation, leading to thermal necrosis of surrounding tissues, blood vessels, and nerves. Addressing these challenges requires innovative cutting techniques that minimize force, control crack propagation, and reduce heat generation while maintaining precise surgical accuracy.

Vibration-assisted cutting (VAC) has emerged as a promising solution to improve bone-cutting efficiency. Studies have shown that elliptical VAC can significantly reduce cutting forces and optimize geometric cutting parameters (Feldmann et al. 2017). Bai et al. (2020) investigated the effects of bone microstructure—including osteons, cement lines, and interstitial matrix—on chip formation and crack propagation, demonstrating that structural heterogeneity influences fracture patterns. Sugita et al. (2017) experimentally confirmed that VAC reduces cutting force by up to 80% compared to conventional cutting. More recently, Shu & Sugita (2020) employed the extended finite element method (XFEM) to analyze crack morphology in cortical bone, showing that VAC effectively

controls crack extension and prevents fractures from fully penetrating the Haversian system.

Despite these advancements, most studies rely on simplified homogeneous bone models, failing to capture the intricate stochastic nature of cortical bone microstructure. The spatial distribution of osteons, cement lines, and Haversian canals significantly affects mechanical behavior, yet many existing models assume uniform distributions, limiting the accuracy and applicability of their findings. Moreover, the relationship between cutting parameters, crack extension mechanisms, and microstructural variability remains poorly understood, highlighting the need for a more precise and computationally efficient approach to model bone-cutting dynamics.

To address these gaps, this study develops a Python-based stochastic modeling framework that incorporates microstructural heterogeneity into finite element models, allowing for precise control over bone porosity and microstructure distribution. Traditional cutting and elliptical VAC are simulated using XFEM to analyze the effects of cutting force, cutting stress, crack propagation, and temperature distribution. By integrating microstructural variability into FEA, this study provides a comprehensive and scalable computational framework for optimizing bone-cutting techniques, offering valuable contributions to both orthopedic surgery and engineering applications.

METHODOLOGY

PYTHON SCRIPTING FOR BONE MICROSTRUCTURE MODELING

At the microscale, cortical bone comprises four microstructural components: Haversian canals, cement lines, osteons, and interstitial fluid. In modeling, the osteons and the Haversian canals are generally regarded as being circular in shape. The modeling process of the microscopic stochastic model of cortical bone involves circular logic which is an iterative process used to generate the stochastic microstructure of cortical bone, particularly the random placement of osteons and Haversian canals while maintaining spatial constraints. In each iterative loop, a new osteon or Haversian canal is generated, positioned, and validated before the next cycle begins. This ensures a controlled yet random distribution that mirrors natural cortical bone microstructure. The overall process can be divided into three parts: pre-processing, circular logic, and post-processing.

Abdel-Wahab et al. (2012) established that the distribution of osteon diameters can be accurately described using the hyper secant distribution curve,

$$f_{hs}(x) = \frac{\operatorname{sech}\left(\frac{\pi(x-\mu)}{2\sigma}\right)}{2\sigma} \quad (1)$$

where $\mu = 35.3$ and $\sigma = 99.9$ are the continuous location and scale parameters, respectively. While the model accounts for the distribution of osteons, cement lines, and the bone matrixSimilarly, the diameters of Haversian canals were characterized using the Dagum distribution, expressed as,

$$f_D(x) = \frac{ak\left(\frac{x-\gamma}{\beta}\right)^{\alpha k-1}}{\beta\left(1+\left(\frac{x-\alpha}{\beta}\right)^{\alpha}\right)^{k+1}} \quad (2)$$

where $k = 1.52$, $\alpha = 2.7$, $\beta = 12.9$, and $\gamma = 3.3$.

The Python script is then developed to determine the random diameter and position distribution of osteon and Haversian canal through the distribution functions. The purpose of this code is to simulate the distribution of Haversian systems within the human skeleton by randomly generating cylindrical structures of varying sizes and positions to achieve a specified proportion of coverage within the simulation region. The geometric parameters of the model are set as in Table 1 following the properties presented in Abdel-Wahab et al. (2012).

The code of the iterative process is illustrated in Figure 1. It is a cycle-based algorithm that begins with initialization, where the dimensions of the simulation domain (e.g., 700 μm × 500 μm) are set along with parameters such as the minimum and maximum osteon diameters, Haversian canal diameters, and cement line spacing. The first osteon is placed at a randomly selected location. Following this, the circular logic cycle is executed, where additional osteons and Haversian canals are generated iteratively. Each new circle (osteon or Haversian canal) is assigned a random diameter and position, ensuring that the spatial distribution mimics natural cortical bone structure.

To maintain biological accuracy, spatial constraints are enforced throughout the iterative process. The algorithm checks whether newly generated osteons and canals overlap existing structures or violate the predefined minimum and maximum separation distances. If a generated structure does not meet these conditions, a new position is calculated, and the process repeats until the constraints are satisfied. This ensures a realistic stochastic arrangement where osteons remain properly spaced and aligned with the bone microstructure.

The cycle continues until one of two termination conditions is met: (1) The cumulative area occupied by osteons and Haversian canals reaches the predefined

proportion of the total domain (e.g., 60%), or (2) The iteration limit is reached to prevent excessive computation time. The final distribution is then used as the basis for finite element analysis (FEA), ensuring that simulations incorporate microstructural features.

While the stochastic model accounts for the distribution of osteons, cement lines, and the bone matrix, it is its simplified representation of the hierarchical complexity of cortical bone that does not explicitly incorporate variations in fiber orientation and mineral content. These factors play a significant role in the mechanical behavior of bones under cutting forces, particularly in fracture propagation and energy dissipation. The study also relies on predefined statistical distributions for osteon and Haversian canal diameters, which may not generalize well to bones from different species, anatomical locations, or pathological conditions.

TABLE 1. Pre-processing script geometry parameters (Abdel-Wahab et al. (2012))

Geometric information	Code terminology	Value
Width	Xlength	700μm
Height	Ylength	500μm
Haversian system	vr	0.6
Minimum distance between cement line and rectangle	bdrec	5μm
Minimum distance between cement lines	bsmin	5μm
Maximum distance between cement lines	bsmax	10μm
Minimum diameter of Haversian canal	idmin	16μm
Maximum diameter of Haversian canal	idmax	25μm
Minimum diameter of osteon	odmin	70μm
Maximum diameter of osteon	odmax	120μm

SCRIPT VALIDATION

To validate the reliability of the Python script, the fracture resistance of the bone model is quantified using the stress intensity factor (k), which is associated with extrinsic toughening mechanisms and governs crack behavior. This parameter is particularly relevant since bone cutting is fundamentally a fracture-driven process, where cracks propagate ahead of the cutting tool. Fracture toughness plays a crucial role in defining a material's resistance to crack propagation, making it essential for evaluating cutting performance and bone integrity.

For this purpose, two finite element models of single-edge notched bend (SENB) specimens were constructed to represent young and aged bones with different microstructural properties. To simplify the model, the stochastic material was applied only near the crack tip where crack is expected to grow, while the rest of the specimen was treated as homogeneous, as illustrated in Figure 2. The fracture toughness tests were simulated following the American Society for Testing and Materials (ASTM E399-90) standard on 10 SENB models representing young and aged bones with different microstructural variations. Each generated model within each group is expected to have a similar k value, ensuring the reliability of the script. The deviation of k value for each model from the reference k—defined as the mean k averaged across all specimens—was calculated and referred to as the error ratio, which is plotted in Figure 3. The figure shows that specimen 1 of both young and aged bones exhibited small error ratio, making them the most representative models for the subsequent analysis of cutting effects in vibration-assisted bone cutting.

Figure 4 displays the generated models of young and aged bones following program execution, with dimensions set to a height of 0.5 mm and a width of 0.7 mm. To minimize the effects of local positional variations, the aged bone model was remodeled based on the young bone model, maintaining the same area distribution of each constituent while incorporating higher porosity. This was achieved by increasing the percentage area of the interstitial matrix and Haversian canals while reducing the percentage area of osteons.

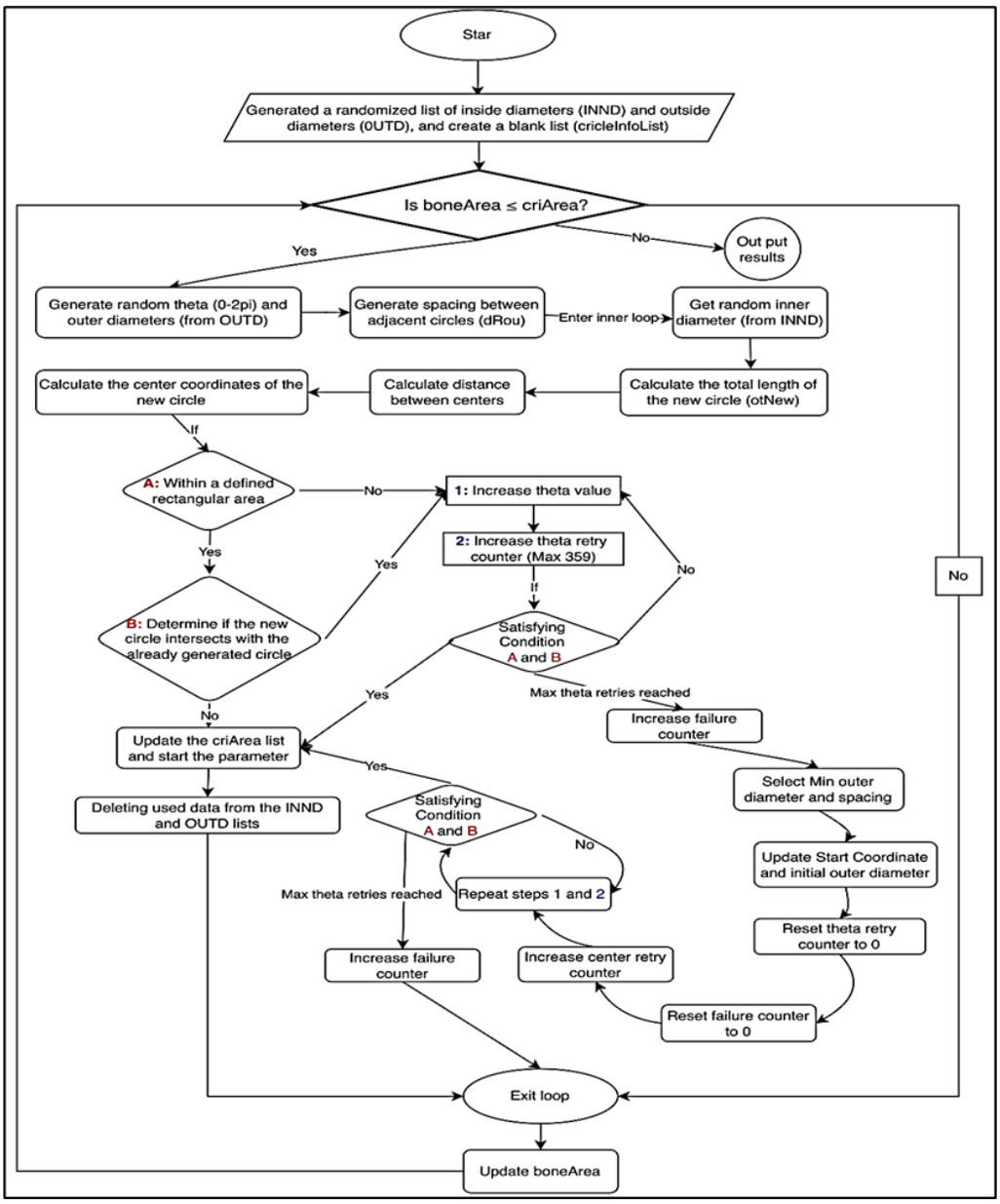

FIGURE 1. Cycle-based algorithm diagram

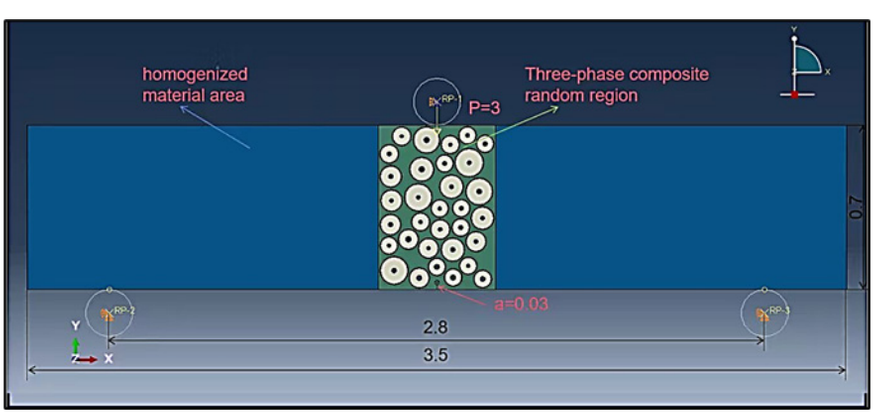

FIGURE 2. Two-dimensional SENB model with a pre-crack

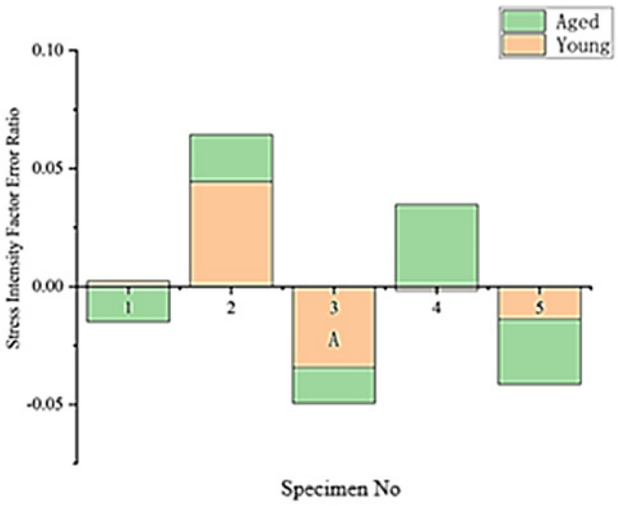

FIGURE 3. Error ratio of stress intensity factor, *k*, for each model

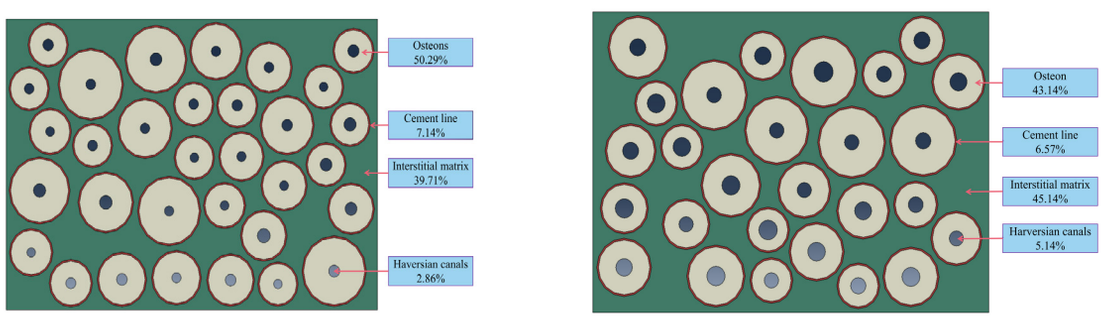

(a) (b)

FIGURE 4. Microstructure distribution of (a) young, and (b) aged bones

FINITE ELEMENT MODELING OF CORTICAL BONE

The finite element (FE) modeling approach employed in this study is designed to accurately represent the mechanical behavior of cortical bone during cutting. The bone material was assumed to be transversely isotropic, which is a reasonable approximation given its hierarchical structure. The material properties used in the model were derived from nanoindentation results reported in Abdel-Wahab et. al (2012), as summarized in Table 2. A strain-based yield criterion of 0.6% strain was chosen to define the onset of plastic deformation, based on its relevance to the bone's mechanical behavior. This threshold was selected in accordance with Abdel-Wahab et. Al (2012) that have demonstrated its suitability in capturing the transition from elastic to plastic response in bone material.

The maximum principal strain criterion (Maxpe) from the traction-separation law was used for damage initiation, while damage evolution was governed by fracture energy. This approach is based on the premise that cracks initiate in regions of highest tensile strain, particularly in brittle materials like cortical bone. The criterion effectively identifies crack initiation zones in materials where tensile failure is the dominant failure mode. A viscosity coefficient of $10e^{-4}$ was applied to prevent computational convergence issues in models with various forms of softening behavior or stiffness degradation (Demir et al (2018).

Contact between the tool and bone occurs at the interface edge OA, as shown in Figure 6, where Haversian systems 1 and 2 are located within the crack extension region. To establish an accurate two-dimensional crack extension model and resolve discontinuities caused by strong cracks and weak interfaces at edge OA, the local mesh in the crack extension region, including Haversian systems 1 and 2, is highly refined, with an approximate element size of 0.002 for the local seed. The entire model was constructed using 4-node bilinear plane strain quadrilateral elements with reduced integration and hourglass control (CPE4R), as shown in Figure 5.

TABLE 2. Material properties of bone microstructure constituents (Abdel-Wahab et al. (2012))

	Osteon	Interstitial	Cement line
Elastic Modulus [GPa]	12.85	14.12	9.64
Poisson's ratio	0.17	0.153	0.49
Yield strain [%]	0.6	0.6	0.6
Fracture initiation strain [%]	0.65	0.65	0.65
Strain energy-release rate [N/m]	860	238	146
Density [kg/m^3]	2000	2000	2000

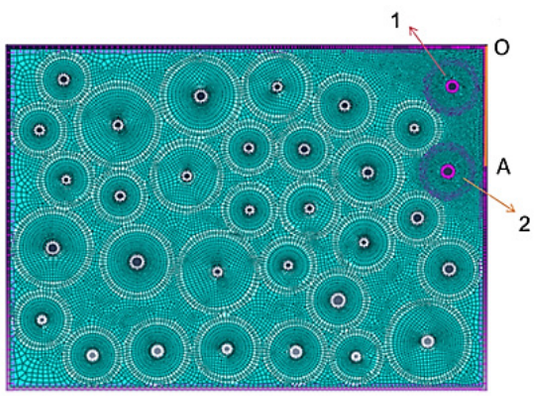

FIGURE 5. Meshed bone model using CPE4R elements

Given that this study pertains to transient analysis and necessitates precise calculation outcomes, the analysis method employs implicit analysis due to its automatic correction capability and large step size, both of which guarantee the accuracy of the calculation results. Fully constrained boundary conditions were imposed on edges AB and BC, with a reference point (RP) set for the tool, as shown in Figure 6. The boundary conditions were set to minimize artificial constraints while maintaining computational efficiency. The tool motion was idealized as a steady state cutting process, neglecting potential fluctuations that might arise in a real cutting environment. The motion conditions were applied at the reference point. In conventional cutting, the tool moves along the x-axis in the negative direction (CB) and is constrained to remain stationary relative to the AB direction using the reference point. In vibration-assisted cutting, the tool moves in an elliptical feed motion along the x-axis in the negative direction (CB), based on a periodic amplitude curve expressed in Fourier series,

$$a = A_0 + \sum_{n=1}^{N} [A_n cosn\omega(t - t_0) + B_n sinn\omega(t - t_0)] \quad (3)$$

where N is the number of terms of the Fourier series, $\omega=2\pi f$ is the circle frequency, t_0 is the starting moment, A_0 is the initial amplitude, A_n is the cosine coefficient, and B_n is the sinusoidal coefficient. After deriving the Fourier series for $N = 1$, and $t_0 = 0$, and assigning the feeding speed v in the negative x-direction, the tool velocity is,

$$x' = A2\pi f sin(2\pi f t) - v \quad (4a)$$

$$y' = B2\pi f cos(2\pi f t) \quad (4b)$$

where x' and y' are the velocities in the x and y direction, and A and B are the vibration amplitudes of the minor axis and major axis, which are initially set as -0.0025 and -0.0075, respectively. Table 3 lists the cutting parameters used for the fracture analysis which are based on experimentally validated values from Shu & Sugita (2020), ensuring the model remains representative of real-world bone-cutting scenarios.

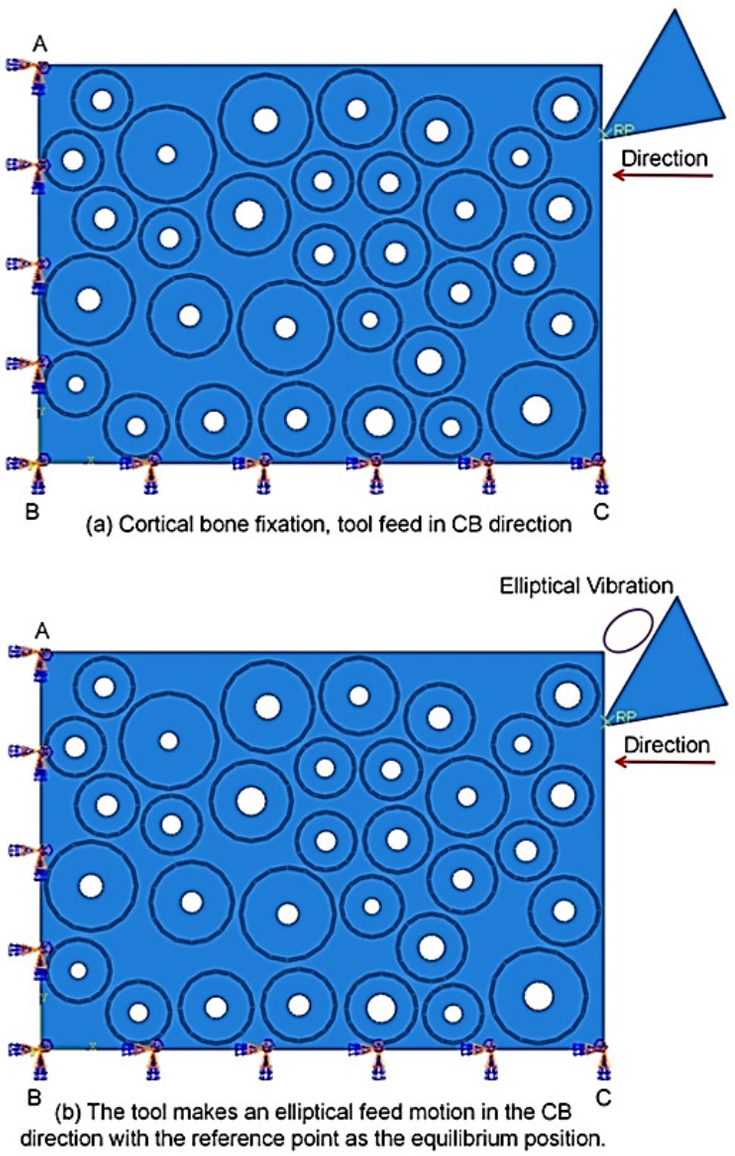

FIGURE 6. The applied dynamic constraints

TABLE 3. The simulation conditions of bone cutting for fracture analysis (Shu & Sugita (2020))

Parameter	Value
Cutting depth [μm]	50,100,150
Rake angle [°]	30
Clearance angle [°]	10
The chamfer of the tip of the tool [μm]	10
Amplitude [μm]	0,5x15
Frequency [Hz]	0,500

BONE MODEL VALIDATION

The developed bone model was validated by numerically measuring the stress intensity factor, k, of the bone and comparing it with publicly available data. For this purpose, a compact tension (CT) specimen model representing the bone was constructed, incorporating its microstructure. The specimen's dimensions followed the ASTM standards, as shown in Figure 7. The load was applied vertically along the y-direction of the material, and k was evaluated and averaged from six contour integrals around the crack tip.

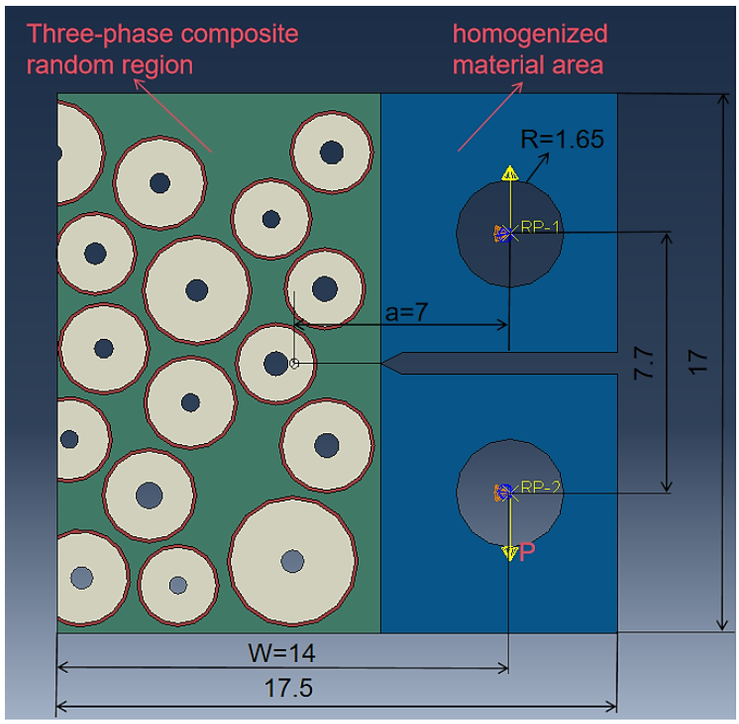

FIGURE 7. Compact tension model with $a/W = 0.5$

As shown in Figure 8, the average k for the young and aged groups was found to be 2.23 $N/mm_{3/2}$ and 2.22 $N/mm_{3/2}$, respectively, with discrepancies of only 11.7% and 7.17% compared to the experimental values reported by Nalla et al. (2005). This agreement between the numerical and experimental results validates the bone model with microstructural elements developed in the present study.

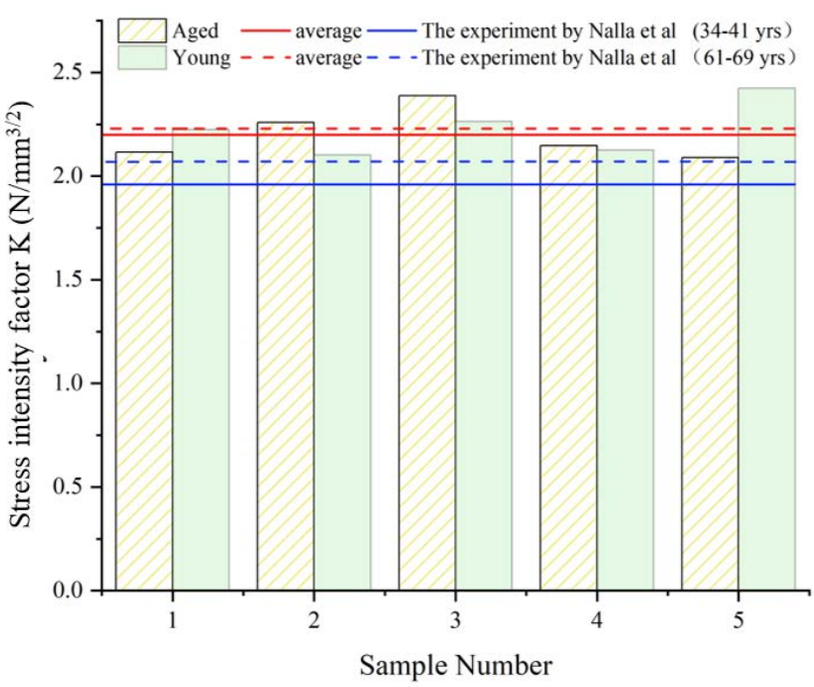

FIGURE 8. The comparison of numerically measured k with the experimental values reported by Nalla et al. (2005)

RESULTS AND DISCUSSION

CUTTING FORCE

The cortical bone of both young and aged groups was cut at depths of 40 µm, 90 µm, and 120 µm to represent distinct structural layers, transitioning from the outer periosteal surface to deeper regions near the Haversian system. Two additional data sets were added near each of these depths (±5 µm) to show mean values, with error bars included. The cutting methods used were conventional cutting, with an amplitude of 0 µm, and vibration-assisted cutting, with amplitudes of 10 µm and 15 µm. The transverse feed was fixed at 5 µm, and the vibration-assisted cutting followed an elliptical path. The results in Figure 10 indicate that the magnitude of the cutting force is directly linked to the amplitude, depth of cut, and the age of the bone tissue being cut. Based on the analysis of the effect of cutting depth on force, the findings of this study align with the experimental results of Tahmasbi et al. (2022). As the depth of cut increases, so does the cutting force, confirming that the depth of cut is the primary factor influencing cutting force magnitude.

Figure 9 also clearly shows that the cutting force in conventional (amplitude 0) cutting is higher than in vibration-assisted cutting at all depths. While vibration-assisted cutting has proven effective in lowering forces, it is interesting to note that Shu & Sugita (2020) found that increasing the amplitude did not have the same effect in reducing cutting forces in the younger group. However, this effect was consistently observed in the aged group.

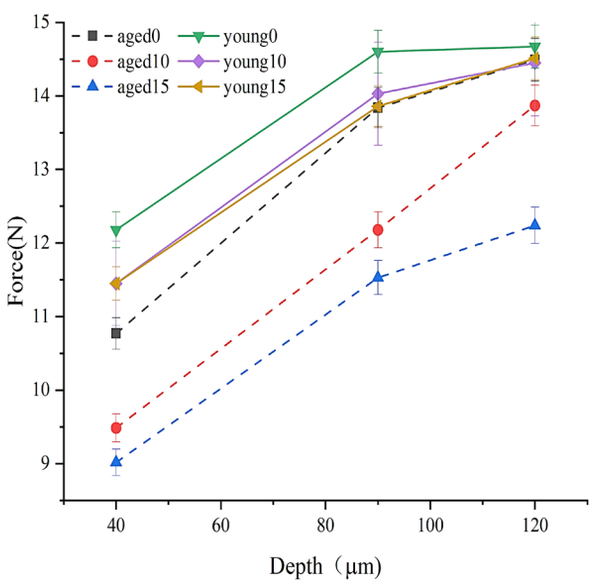

FIGURE 9. Cutting force at different cutting amplitudes and cutting depths for aged and young bones

Gustafsson et al. (2019) investigated the impact of varying porosities on interfacial damage and analyzed the resulting force-displacement curves. It was observed that peak force decreased as porosity increased, based on multiple sets of model data ranging from 2% to 15% porosity. Similarly, in the current study, the aged group consistently exhibited lower cutting forces compared to the younger group, regardless of the cutting method used. However, the aged group showed a greater increase in cutting force than the younger group as depth increased. For example, with a cutting amplitude of 10 µm, the aged group's cutting force increased from 9.38 N at a depth of 40 µm to 13.65 N at 120 µm, an increment of 4.27 N. In contrast, the young group experienced a rise from 11.43 N at 40 µm to 14.29 N at 120 µm, resulting in an increment of 2.86 N. This indicates a 30.6% decrease in the cutting force for the young group compared to the aged group as depth increased. This trend remained consistent across both groups when using an amplitude of 15 µm and in the absence of vibration. Therefore, it can be deduced that the cutting force in the aged group was more affected by depth and exhibited greater instability.

This finding introduces another important factor to consider when designing or using a vibration-assisted cutting device. Shu & Sugita (2020) suggested that a larger vibration amplitude is preferable for generating a pulsating cutting force, which reduces the energy required for bone removal. However, when accounting for bone porosity, a high amplitude will significantly affect only bones with higher porosity. Therefore, in future designs and applications of vibration-assisted cutting devices, it is crucial to consider bone porosity when selecting the amplitude size.

CUTTING STRESS

The generated cutting stress is assessed in terms of Von Mises stress, given its ability to account for the multi-axial stress state when evaluating the overall failure behavior of materials under complex loading conditions. Figure 10 shows the maximum Mises stress in bone tissue at different cutting depths (40, 90, and 120 µm) and amplitudes (0, 10, and 15 µm) for both young and aged groups. Except for the 120 µm depth in the young group, the maximum Mises stress during vibration-assisted cutting is consistently lower than that of conventional cutting, regardless of cutting depth.

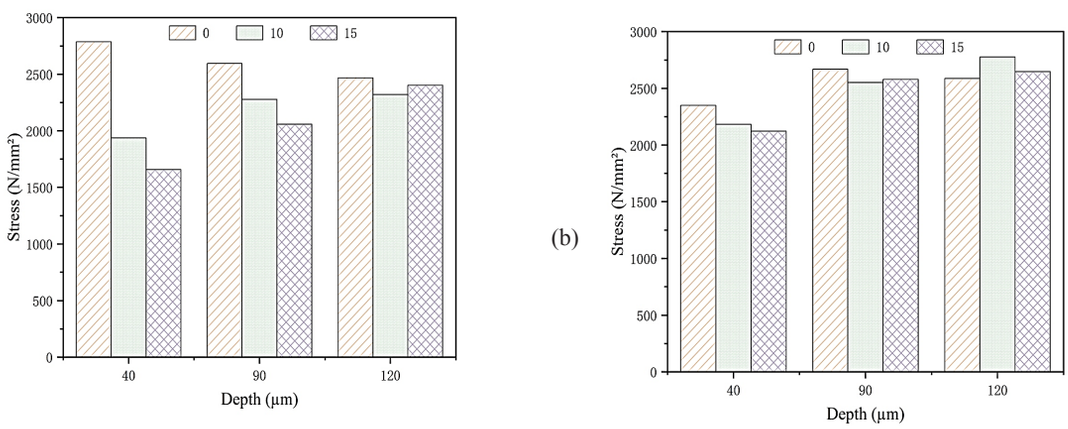

(a) (b)

FIGURE 10. Von Mises stress at different cutting amplitudes and cutting depths for (a) aged, and (b) young bones

As shown in Figure 11, the difference in stress values between the conventional and elliptical cutting is largest for the lowest cutting depth, 40 µm, when the Mises stress reaches 40.6% in the older group and 9.63% in the younger group. As the cutting depth increased, the difference in stress values between the two cutting methods gradually decreased. Slope M reflects the effect of cutting depth on the performance of vibration-assisted cutting; the difference in cutting stress between the two cutting methods decreases as depth increases, and the slope of the trend line can be quantified as approximately M_e = -0.309 for the aged group and M_y = -0.0875 for the young group.

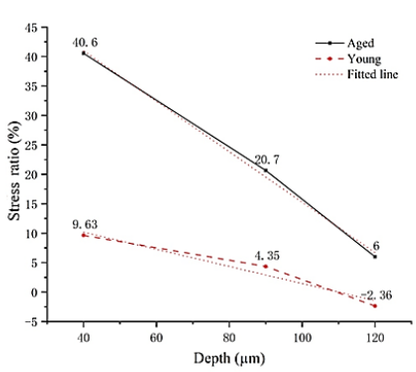

FIGURE 11. Percentage difference of maximum Von Mises stress between VAC and conventional cuttings for aged and young bones

Gustafsson et al. (2019) demonstrated that increased cortical bone porosity leads to a reduction in both structural stiffness and peak force, while enhancing the bone's ability to absorb energy before failure. As structural stiffness decreases, the material becomes less resistant to deformation, which in turn lowers the peak force it can withstand. This reduction in stiffness and peak force directly influences how the bone absorbs and dissipates energy under stress. In line with the present findings, the younger group exhibited higher Mises stresses compared to the older group, reflecting the greater stiffness and lower porosity of younger bone, which enables it to sustain higher stresses before yielding. However, in conventional cutting, the older group displayed higher Mises stress at 40 µm cutting depth. This suggests that the reduction in stiffness with age and increased porosity not only affects the material's peak force but also alters its response to localized stresses.

CRACK PROPAGATION

Figures 12, 13, and 14 illustrate the crack propagation patterns in aged and young bone models at three different cutting amplitudes for cutting depths of 40 µm, 90 µm, and 120 µm, respectively. It has been observed that cracks tend to follow the cement line, which plays a critical role in the fracture process by protecting the entire Haversian system (Giner et al. 2017). This behavior is particularly evident in the conventional cutting model, where cracks either propagate or deflect along the cement line, as shown in the figures. However, in vibration-assisted cutting, the larger diameter of the Haversian canal becomes more influential, attracting the crack and causing it to deflect upward and backward, as demonstrated in the figures.

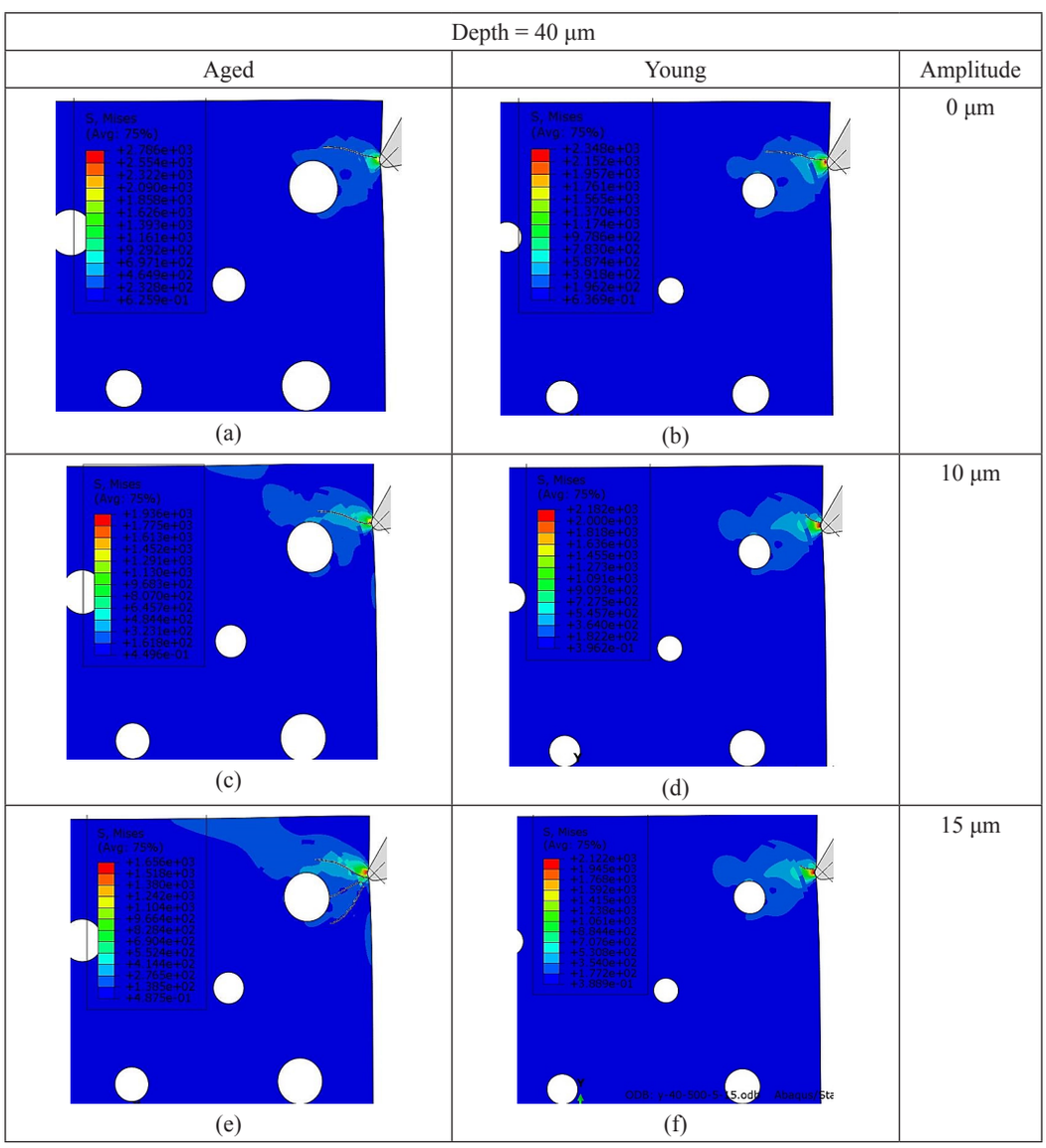

FIGURE 12. Crack propagation patterns in aged and young bones at varying amplitudes for a cutting depth of 40 µm

When comparing the aged and young groups in conventional cutting, the direction of crack propagation is nearly identical. However, the crack length in the younger group is slightly shorter than in the older group. This trend is consistent for all cutting depths. In shallow cutting, cracks tend to follow the cement line, and as the depth increases, they continue to propagate downward, occasionally altering direction toward the cement line. This confirms that the cement line plays a crucial role in crack propagation in cortical bone, as claimed by Li et al. (2013).

In the young group, vibration-assisted cutting effectively controlled crack propagation at the cutting depth of 40 µm, resulting in smoother crack paths and higher-quality bone surfaces compared to conventional cutting. Conventional cutting caused vertical cracks that crossed the cement line, while vibration-assisted cutting caused cracks to deflect upward and backward near the cement line, which is consistent with Shu & Sugita (2020).

At the cutting depth of 90 µm, cracks from conventional cutting followed the cement line. In contrast, small-amplitude vibration-assisted cutting caused cracks to deflect upward and backward, ceasing propagation once they crossed the cement line. Large-amplitude vibration-assisted cutting, however, deflected the cracks upward, and they continued to propagate within the osteon after crossing the cement line.

At the cutting depth of 120 µm, cracks from conventional cutting propagated downward, while those from vibration-assisted cutting moved upward and backward. Interestingly, none of the cracks crossed the cement line at this depth. It was also observed that cracks had a greater inclination for small-amplitude cuts compared to large-amplitude cuts, with the crack paths appearing smoother.

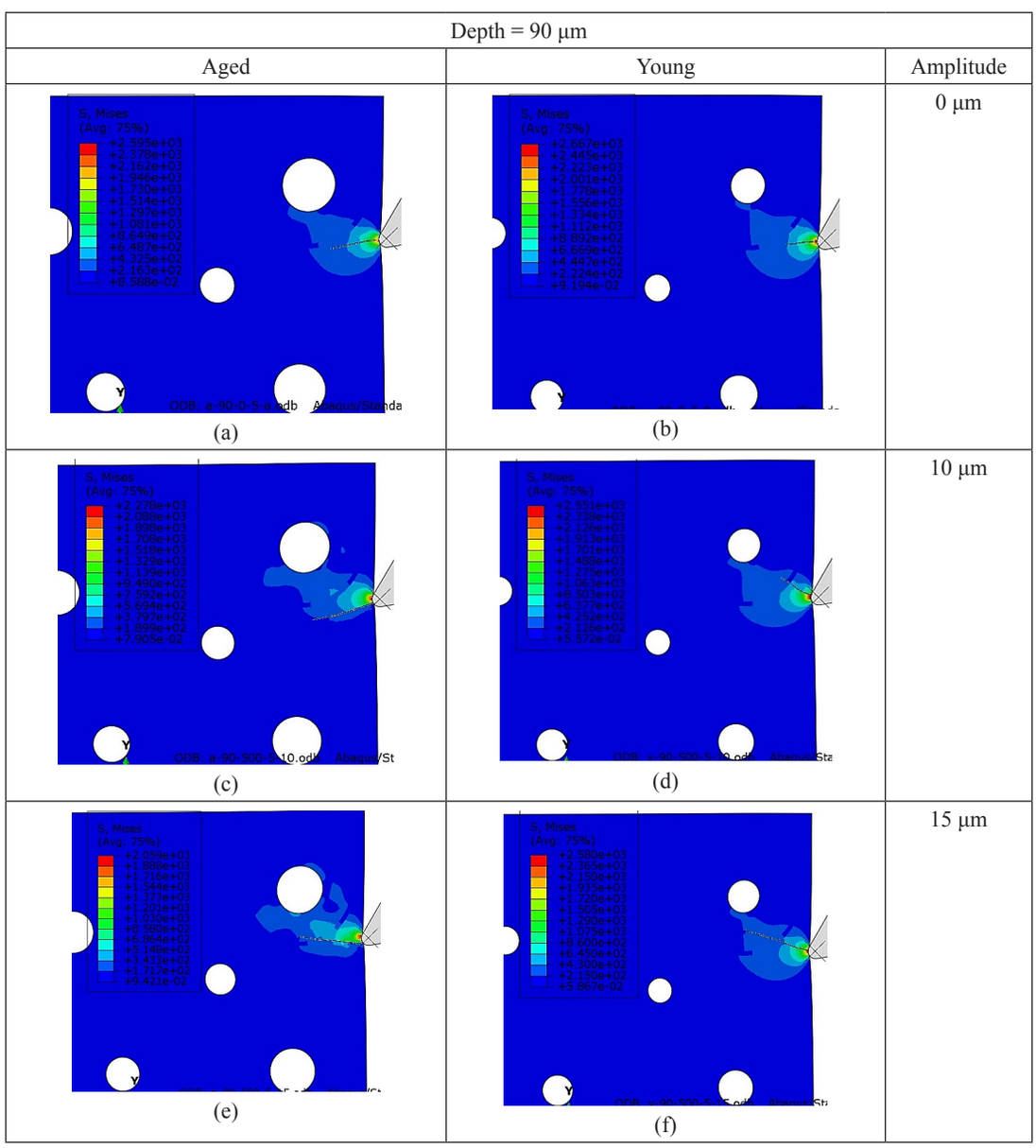

FIGURE 13. Crack propagation patterns in aged and young bones at varying amplitudes for a cutting depth of 90 µm

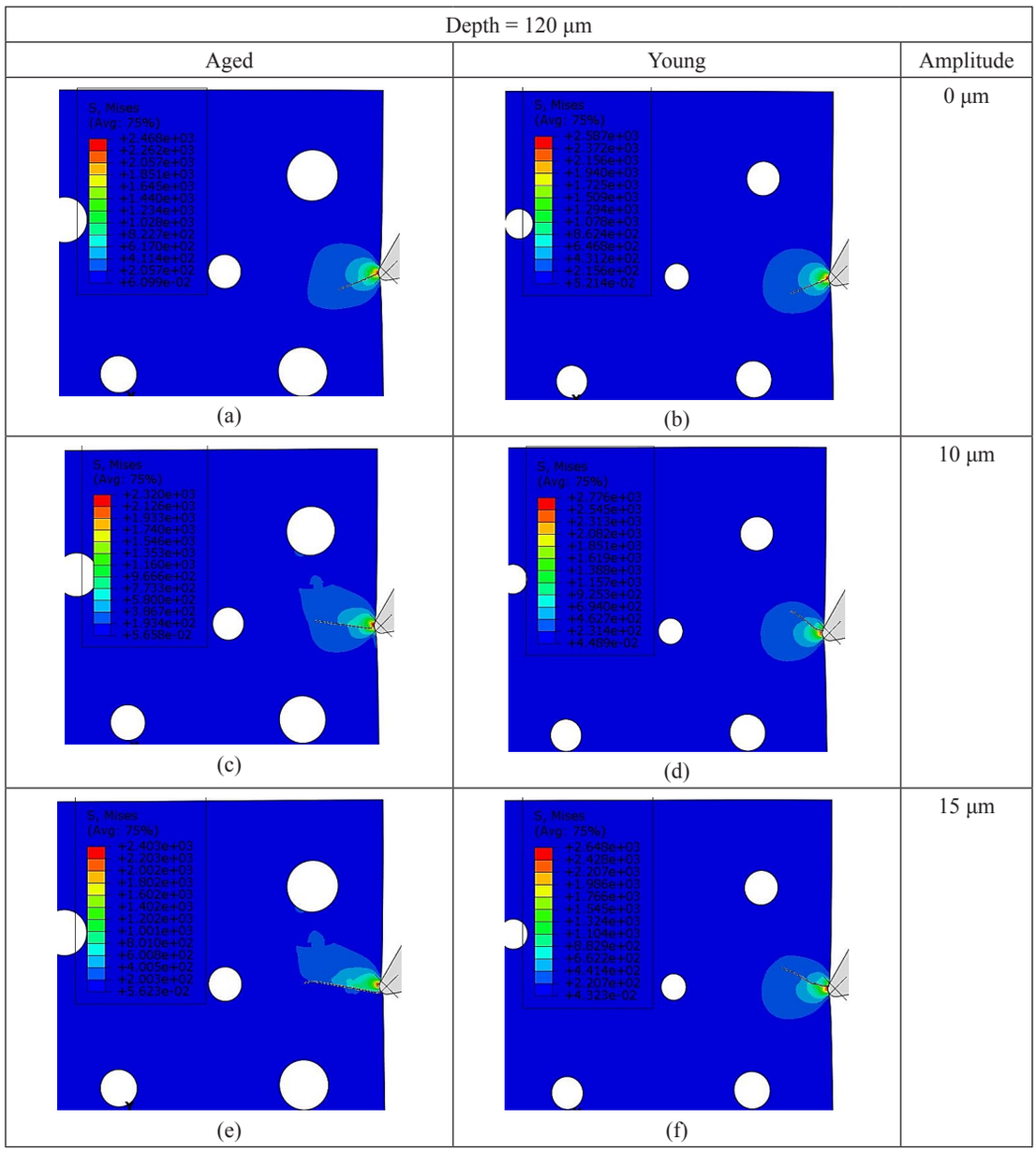

FIGURE 14. Crack propagation patterns in aged and young bones at varying amplitudes for a cutting depth of 120 µm

CUTTING TEMPERATURE

To investigate the effect of elliptical vibration-assisted cutting on cutting temperature, a thermodynamically coupled finite element model was developed. This model allows for the simulation of temperature rise in bone material. The two cutting methods were compared to observe their impact on temperature increase. The thermodynamic parameters are listed in Table 4, and the initial temperature was set to 37 °C, the normal temperature of the human body. The temperature of young cortical bone was simulated for both elliptical vibration-assisted cutting and conventional cutting.

TABLE 4. Material properties of cortical bone used in simulations (Alam et al. 2010).

Property	Value
Thermal conductivity (W/m K)	0.56
Heat capacity (J/kg K)	1260
Mechanical parameters	Refer to Table 2

In the present work, the bone tissue was treated using the strain-rate sensitive Johnson-Cook (JC) material model. The model is presented as having been effectively used for bone cutting modeling in the past.

$$\sigma_Y = \left(A + B\varepsilon_p{}^n\right)\left[1 + C\ln\left(\frac{\dot{\varepsilon}_p}{\dot{\varepsilon}_o}\right)\right]\left[1 - \frac{(T - T_O)}{(T_{melt} - T_0)}\right]^m \quad (5)$$

where A, B, C, n and m are constants, σ_Y is the yield stress, ε_p is the plastic strain, $\dot{\varepsilon}_p$ is the effective plastic strain rate, $\dot{\varepsilon}_o$ is the reference strain rate, T_o is the initial temperature, T_{melt} is the material melting point, and T is the surface temperature. The JC parameters used in the simulations are given in Table 5.

TABLE 5. Johnson-Cook parameters used in cutting simulations

A (MPa)	B (MPa)	C	n	m	T_{melt} (K)
50	101	0.03	0.08	1.03	875

As shown in Figure 15, elliptical vibration-assisted cutting results in higher cutting temperatures compared to conventional cutting. This is due to the increased friction and periodic impacts between the bone and the tool. However, in terms of heat transfer distribution, the high-temperature region in vibration-assisted cutting is significantly smaller than that of conventional cutting, making it easier for bone tissue to form cutting chips. Once a chip is fully formed, it carries away a large amount of heat. Since the chip is no longer part of the bone, its temperature becomes negligible, which helps reduce the temperature of the remaining bone tissue.

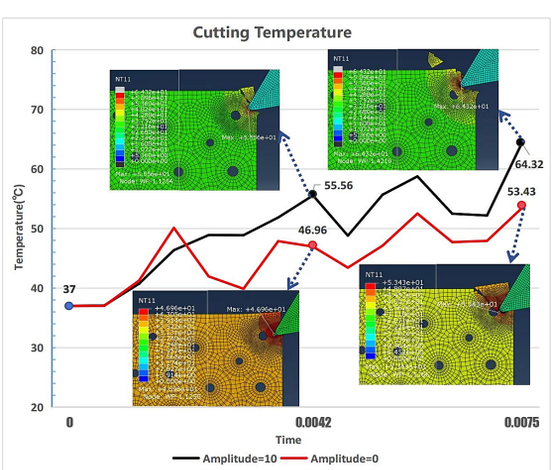

FIGURE 15. Cutting temperature for VAC at 10 µm compared to conventional cutting

CONCLUSION

This study uses XFEM numerical simulations to compare elliptical vibration-assisted cutting with conventional cutting of cortical bone, aiming to optimize orthopedic surgery by reducing cutting forces, improving surface quality, and facilitating chip formation. This study also examines the influence of bone mechanical properties and age-related increases in microscopic porosity (Hunter & Agnew, 2016) as fracture risk rises with age, largely due to bone loss and changes in bone microstructure (Burr, 2019).

A Python-based stochastic model was employed to randomize geometric parameters and microstructural positions. Since the local positioning of bone osteons relative to the cutting tool significantly affects crack propagation, the osteon's position in the model was kept constant. For the aged group, only porosity was increased to simulate age-related changes. Validation through a SENB model demonstrated that the stress intensity factor k was within a 5% error margin, indicating minimal influence from microstructural positioning. Further validation with compact tensile models showed strong agreement between numerical and experimental k values, confirming the accuracy of the bone model with microstructural elements developed in this study.

The XFEM analysis reveals that increasing bone porosity under the same load results in higher stress intensity. The analysis further shows that VAC significantly reduces cutting force and stress. Operations with a larger amplitude have been reported to effectively reduce cutting forces (Shu & Sugita, 2020); however, this effect appears to be most pronounced in aged bone with high porosity and shows minimal impact on young bone with lower porosity. These findings highlight the importance of considering both operating amplitude and specific bone properties to ensure effective bone-cutting procedures.

Regarding crack propagation, it is demonstrated to be more controlled in vibration-assisted cutting. The young group exhibites greater resistance to cracking, particularly during the crack initiation stage, influenced by the distribution and area relationships within the Haversian system. In contrast, damage evolution in the aged group is dominated by the osteon areal fraction, which has an intrinsically high strain-energy release rate. This higher osteon areal fraction in the young group further enhances its load-bearing capacity (Wang et al. 2020).

Lastly, the thermo-mechanical coupling models indicates that while vibration-assisted cutting produces higher maximum temperatures than conventional cutting, the high-temperature zone remains more localized near the tool. This demonstrates the effective heat dissipation of

VAC, which may lead to the generation of smaller cutting chips.

ACKNOWLEDGEMENT

The authors would like to acknowledge the support from the Ministry of Higher Education Malaysia under the Fundamental Research Grant Scheme: FRGS/1/2021/TK0/USM/02/15.

DECLARATION OF COMPETING INTEREST

None

REFERENCES

Abdel-Wahab, A.A., Maligno, A.R., & Silberschmidt, V.V. 2012. Micro-scale modelling of bovine cortical bone fracture: Analysis of crack propagation and microstructure using X-FEM. Computational Materials Science 52(1): 128–135.

Alam, K., Mitrofanov, A.V., & Silberschmidt, V.V. 2010. Thermal analysis of orthogonal cutting of cortical bone using finite element simulations. International Journal of Experimental and Computational Biomechanics 1(3): 236-251.

Bai, W., Shu, L., Sun, R., Xu, J., Silberschmidt, V.V., & Sugita, N. 2020. Improvements of material removal in cortical bone via impact cutting method. Journal of Mechanical Behavior of Biomedical Materials 108: 103791.

Burr, D.B. 2018. Changes in bone matrix properties with aging. Bone 120: 85–93.

Demir, A., Ozturk, H., Edip, K., Stojmanovska, M., Bogdanovic, A. 2018. Effect of viscosity parameter on the numerical simulation of reinforced concrete deep beam behavior. The Online Journal of Science and Technology 8: 50-56.

Feldmann, A., Ganser, P., Nolte, L. & Zysset, P. 2017. Orthogonal cutting of cortical bone: Temperature elevation and fracture toughness. International Journal of Machine Tools & Manufacture 118–119: 1–11.

Giner, E., Belda, R., Arango, C., Vercher-Martínez, A., Tarancón, J.E., & Fuenmayor, F.J. 2017. Calculation of the critical energy release rate Gc of the cement line in cortical bone combining experimental tests and finite element models. Engineering Fracture Mechanics 184: 168–182.

Gustafsson, A., Wallin, M., & Isaksson, H. 2019. Age-related properties at the microscale affect crack propagation in cortical bone. Journal of Biomechanics 95: 109326.

Hunter, R.L., & Agnew, A.M. 2016. Intraskeletal variation in human cortical osteocyte lacunar density: Implications for bone quality assessment. Bone Reports 5: 252–261.

Li, S., Abdel-Wahab, A.A., & Silberschmidt, V.V. 2013. Analysis of fracture processes in cortical bone tissue. Engineering Fracture Mechanics 110: 448–458.

Lin, Z.X., Xu, Z.H., An, Y.H. & Li, X. 2016. In situ observation of fracture behavior of canine cortical bone under bending. Materials Science and Engineering C 62: 361–367.

Nalla, R.K., Kruzic, J.J., Kinney, J.H., & Ritchie, R.O. 2005. Mechanistic aspects of fracture and R-curve behavior in human cortical bone. Biomaterials 26(2): 217–231.

Robles-Linares, J.A., Axinte, D., Liao, Z., & Gameros, A. 2021. Machining-induced thermal damage in cortical bone: Necrosis and micro-mechanical integrity. Materials & Design 197: 109215.

Shu, L., & Sugita, N. 2020. Analysis of fracture, force, and temperature in orthogonal elliptical vibration-assisted bone cutting. Journal of Mechanical Behavior of Biomedical Materials 103: 103599.

Sugita, N., Shu, L., Shimada, T., Oshima, M., Kizaki, T., & M. Mitsuishi, M. 2017. Novel surgical machining via an impact cutting method based on fracture analysis with a discontinuum bone model. CIRP Annals - Manufacturing Technology 66 (1): 65–68.

Tahmasbi, V., Qasemi, M., Ghasemi, R., & Gholami, R. 2022. Experimental study and sensitivity analysis of force behavior in cortical bone milling. Medical Engineering & Physics 105: 103821.

Wang, M., Li, S., Scheidt, A.V., Qwamizadeh, M., Busse, B. & Silberschmidt, V.V. 2020. Numerical study of crack initiation and growth in human cortical bone: Effect of micro-morphology. Engineering Fracture Mechanics 232: 107051.